

# Constraining primordial non-Gaussianity using two galaxy surveys and CMB lensing

Mario Ballardini<sup>1,2\*</sup>, William L. Matthewson<sup>1†</sup>, Roy Maartens<sup>1,3‡</sup>

<sup>1</sup>*Department of Physics & Astronomy, University of the Western Cape, Cape Town 7535, South Africa*

<sup>2</sup>*INAF/OAS Bologna, via Gobetti 101, I-40129 Bologna, Italy*

<sup>3</sup>*Institute of Cosmology & Gravitation, University of Portsmouth, Portsmouth PO1 3FX, UK*

12 June 2019

## ABSTRACT

Next-generation galaxy surveys will be able to measure perturbations on scales beyond the equality scale. On these ultra-large scales, primordial non-Gaussianity leaves signatures that can shed light on the mechanism by which perturbations in the early Universe are generated. We perform a forecast analysis for constraining local type non-Gaussianity and its two-parameter extension with a simple scale-dependence. We combine different future galaxy surveys – a 21cm intensity mapping survey and two photometric galaxy surveys – via the multi-tracer approach. Furthermore we then include CMB lensing from a CMB Stage 4 experiment in the multi-tracer, which can improve the constraints on bias parameters. We forecast  $\sigma(f_{\text{NL}}) \simeq 0.9$  (1.4) by combining SKA1, a Euclid-like (LSST-like) survey, and CMB-S4 lensing. With CMB lensing, the precision on  $f_{\text{NL}}$  improves by up to a factor of 2, showing that a joint analysis is important. In the case with running of  $f_{\text{NL}}$ , our results show that the combination of upcoming cosmological surveys could achieve  $\sigma(n_{\text{NL}}) \simeq 0.12$  (0.22) on the running index.

**Key words:** large-scale structure of Universe – cosmological parameters – early Universe

## 1 INTRODUCTION

The coherent nature of the cosmic microwave background (CMB) anisotropies and the large-scale structure (LSS) we observe around us suggests that the seed for these fluctuations were created at very early times, possibly during a period of inflation (Starobinsky 1980; Guth 1981; Sato 1981; Linde 1982; Albrecht & Steinhardt 1982; Hawking et al. 1982; Linde 1983; Mukhanov & Chibisov 1981).

Inflation observables are predicted to be proportional to the slow-roll parameters for the single field slow-roll (SFSR) models and to be connected through consistency relations for this simplest class of models. For this reason, in the absence of any salient features in the primordial power spectrum, which might open a new observational window on high energy physics happening in the early Universe (Chen et al. 2015), SFSR constraints in the next decade will likely be limited to improvements to the constraints on the scalar spectral index and the tensor-to-scalar ratio. The prospects of detecting the running of the scalar spectral index, that arises in SFSR models at second-order in slow-roll param-

eters ( $dn_s/d \ln k \propto (n_s - 1)^2$ ), may be nearly impossible even with next-generation cosmological surveys (Ballardini et al. 2016; Muñoz et al. 2017; Li et al. 2018; Mifsud & van de Bruck 2019).

One additional observational probe that allows us access to early-Universe physics is primordial non-Gaussianity (PNG) (see Bartolo et al. 2004; Chen 2010, for reviews). The PNG parameter  $f_{\text{NL}}$  is predicted to be first order in slow-roll from consistency relations for SFSR model,  $f_{\text{NL}} \simeq -5(n_s - 1)/12$  (Acquaviva et al. 2003; Maldacena 2003; Creminelli & Zaldarriaga 2004). On the other hand, an  $f_{\text{NL}} \gtrsim 1$  is expected for many multi-field inflation models (see Byrnes & Choi (2010) for a review).

At present, the best constraints on PNG come from *Planck* measurements of the three-point correlation function of the CMB temperature and polarization anisotropies (Akrami et al. 2019), but LSS is emerging as a promising complementary observable. Nonlinear mode coupling from local PNG induces a modulation of the local short-scale power spectrum through a scale dependence in the bias produced by the long-wavelength primordial gravitational potential  $\Phi$  (Salopek & Bond 1990; Gangui et al. 1994)

$$\Phi(\mathbf{x}) = \phi(\mathbf{x}) + f_{\text{NL}} \left( \phi^2(\mathbf{x}) - \langle \phi^2 \rangle \right) + \mathcal{O}(\phi^3) \quad (1)$$

\* Contact e-mail: [mario.ballardini@gmail.com](mailto:mario.ballardini@gmail.com)

† Contact e-mail: [willmatt4th@gmail.com](mailto:willmatt4th@gmail.com)

‡ Contact e-mail: [roy.maartens@gmail.com](mailto:roy.maartens@gmail.com)

where  $\phi$  is a Gaussian field. The appearance of  $\Phi$  in the halo bias implies a specific form of scale-dependence that cannot be created dynamically (i.e. by late time processes).

This is the main reason that halo bias is such a robust probe of the initial conditions and this gives us the opportunity to study PNG with two-point statistics of the LSS. Crucially, the  $k^{-2}$  scaling which arises for some *local* model of PNG makes the signal largest on the very largest scales of the matter power spectrum (Dalal et al. 2008; Matarrese & Verde 2008; Desjacques et al. 2009; Slosar et al. 2008; Camera et al. 2013). Such large scales, greater than the equality scale, are affected strongly by cosmic variance, which puts a fundamental limit on the precision with which  $f_{\text{NL}}$  can be measured (Alonso et al. 2015).

A novel proposal to improve the expected constraints on the amplitude of the PNG fluctuations is to combine the information coming from different LSS tracers or to split the sample in bins of different halo mass in order to reduce the sample variance (Seljak 2009; Yoo et al. 2012; Abramo & Leonard 2013; Ferramacho et al. 2014; Yamauchi et al. 2014; Ferraro & Smith 2015; de Putter & Doré 2017; Alonso & Ferreira 2015; Fonseca et al. 2015, 2017; Abramo & Bertacca 2017; Fonseca et al. 2018). This is the so-called *multi-tracer* approach. Moreover, the cross-correlation between clustering and CMB lensing has recently been shown to be particularly well-suited to measure local PNG using the scale-dependent halo bias (Schmittfull & Seljak 2018).

Currently, the tightest constraints on local type PNG are  $f_{\text{NL}} = -0.9 \pm 5.1$  at 68% CL from the *Planck* 2018 data (Akrami et al. 2019), and  $-51 < f_{\text{NL}} < 21$  at 95% CL from eBOSS DR14 data (Castorina et al. 2019).

This paper aims to assess the constraining power achievable by a multi-tracer combination of two next-generation galaxy surveys and a CMB Stage 4 (CMB-S4) survey.

We consider also a generalization of the  $f_{\text{NL}}$ -model (1), in which the parameter  $f_{\text{NL}}$  is promoted to a function of scale  $k$  (Chen 2005; Sefusatti et al. 2009; Raccanelli et al. 2015)

$$f_{\text{NL}}(k) = f_{\text{NL}} \left( \frac{k}{k_{\text{piv}}} \right)^{n_{\text{NL}}}, \quad (2)$$

where  $k_{\text{piv}}$  is some pivot scale fixed at 0.035 h/Mpc. The tightest current observational constraint on the running index is from the bispectra of the CMB fluctuations:  $0.6 < n_{\text{NL}} < 1.4$  at 68% CL from WMAP9 data, for the single-field curvaton scenario (Becker & Huterer 2012; Oppizzi et al. 2018).

This paper is organized as follows: in section 2 we describe how the different PNG templates enter into the halo bias through a scale-dependent contribution. We then describe the cosmological surveys considered in our analysis: CMB-S4 as a CMB experiment, SKA1-MID Band 1 IM, and as LSS experiments: Euclid-like and LSST-like. In section 3. We also introduce the Fisher forecasting formalism in section 3. Finally, we present our results in section 4 and we draw our conclusion in section 5.

## 2 PRIMORDIAL NON-GAUSSIANITY AND LARGE SCALE STRUCTURE

In this section we describe the large-scale halo bias in the context of the peak-background split (PBS) (Mo & White 1996; Sheth & Tormen 1999; Schmidt & Kamionkowski 2010; Desjacques et al. 2018). The PBS method is used to predict the large-scale clustering statistics of dark matter halos. The Gaussian field is split into long- and short-scale modes  $\phi = \phi_\ell + \phi_s$ , where the long scales determine the clustering of halos relevant for large-scale power spectrum analysis, while the short scales specify the halo formation.

In order to connect the matter density contrast  $\delta$  to the gravitational potential  $\Phi$ , we make use of the Poisson equation at late times

$$\nabla^2 \Phi = -\frac{3}{2} \Omega_{m,0} H_0^2 \frac{\delta}{a} \quad (3)$$

where the potential has been defined under the following convention for the perturbed metric in the Newtonian gauge

$$a^{-2} ds^2 = (1 + 2\Psi) d\eta^2 - (1 - 2\Phi) dx_i dx^i. \quad (4)$$

At late times the gravitational potential  $\Phi$  can be connected to the primordial potential  $\Phi_p$  by

$$\Phi(k, z) = \frac{T(k) \Phi_p(k) D(z)}{a(z)} \quad (5)$$

where  $T(k)$  is the matter transfer function normalized to one at large scales, and  $D(z)$  is the growth factor normalized to the scale factor in the matter-dominated era.

From the Poisson Eq. (3), we can write the matter density contrast as

$$\delta(\mathbf{k}, z) = \alpha(k, z) \Phi_p(\mathbf{k}) \quad (6)$$

with

$$\alpha(k, z) \equiv \frac{2k^2 T(k) D(z)}{3\Omega_{m,0} H_0^2}. \quad (7)$$

In presence of local PNG of the form in Eq. (1), the Laplacian of the primordial potential is

$$\nabla^2 \Phi \simeq \nabla^2 \phi + 2f_{\text{NL}} \left( \phi \nabla^2 \phi + |\nabla \phi|^2 \right) \quad (8)$$

and we can split its contribution into long and short wavelengths at leading order as

$$\Phi_\ell \simeq \phi_\ell, \quad (9)$$

$$\Phi_s \simeq \phi_s (1 + 2f_{\text{NL}} \phi_\ell). \quad (10)$$

The long-wavelength overdensity  $\delta_\ell$  which describes the clustering properties of the matter distribution is not affected by the presence of PNG

$$\delta_\ell(\mathbf{k}, z) = \alpha(k, z) \phi_\ell(\mathbf{k}), \quad (11)$$

while the short-wavelength fluctuations are altered by long wavelengths. At lowest order neglecting white-noise contributions, we have

$$\delta_s(\mathbf{k}) = \alpha(k, z) \phi_s(\mathbf{k}) (1 + 2f_{\text{NL}} \phi_\ell). \quad (12)$$

The local number density of halos in Lagrangian space is given by

$$n_h = \bar{n}_h (1 + b_L \delta_\ell) \quad (13)$$

where  $b_L$  stands for Lagrangian-space bias,  $\delta_\ell$  is again the contribution from the long-wavelength modes in (10) that essentially modulate the mean density of the effective local cosmology. Therefore

$$b_L = \frac{d \ln n_h}{d \delta_\ell} \quad (14)$$

and the more usual Eulerian-space bias is given by  $b_0 = 1 + b_L$ .

In the presence of PNG, the local number of halos does not just depend on the large-scale matter perturbations, but it is also affected by the mode coupling between long and short wavelengths that acts like a local rescaling of the amplitude of (small-scale) matter fluctuations. Taylor expanding at first order in these parameters

$$\begin{aligned} b_L &= \frac{d \ln n_h}{d \delta_\ell} \\ &= \frac{\partial \ln n_h}{\partial \delta_\ell} \\ &\quad + \frac{\partial(1 + 2f_{\text{NL}}\phi_\ell)}{\partial \phi_\ell} \frac{\partial \phi_\ell}{\partial \delta_\ell} \frac{\partial \ln n_h}{\partial(1 + 2f_{\text{NL}}\phi_\ell)} \\ &= \frac{\partial \ln n_h}{\partial \delta_\ell} + \frac{2f_{\text{NL}}}{\alpha(k, z)} \frac{\partial \ln n_h}{\partial \ln \sigma_8^{\text{loc}}} \end{aligned} \quad (15)$$

$$= b_L^{\text{Gauss}} + \Delta b(k, z) \quad (16)$$

where we parametrize the local amplitude of small-scale fluctuations with  $\sigma_8^{\text{loc}} = \sigma_8(1 + 2f_{\text{NL}}\phi_\ell)$ , and we introduce the scale-dependent contribution to the large-scale bias as

$$\Delta b(k, z) = f_{\text{NL}} \frac{\beta_f}{\alpha(k, z)}. \quad (17)$$

Finally, on large scales we can relate the halo density contrast to the linear density field as

$$\delta_h(\mathbf{k}, z) = [b_0(z) + \Delta b(k, z)] \delta(\mathbf{k}, z) \quad (18)$$

where  $b_0 = 1 + b_L^{\text{Gauss}}$  is the Eulerian-space bias connected to the Gaussian Lagrangian-space bias.

Throughout this paper, we will use the expression  $\beta_f = 2\delta_c(b_0 - 1)$ , which is exact in a barrier crossing model with barrier height  $\delta_c$  and is a good ( $\approx 10\%$  accuracy) fit to N-body simulations (Dalal et al. 2008). We see that, unlike the Gaussian linear bias  $b_0$ , the non-Gaussian linear bias will no longer be scale-independent, correcting  $b_0$  by a factor  $\propto f_{\text{NL}}/k^2$ .

Note that there are two conventions to define  $f_{\text{NL}}$  in Eq. (1): the LSS convention where  $\Phi$  is normalized at  $z = 0$ , and the CMB convention where  $\Phi$  is instead the primordial potential. The relation between the two normalizations is

$$f_{\text{NL}}^{\text{LSS}} = \frac{D(z = \infty)(1 + z)}{D(z = 0)} f_{\text{NL}}^{\text{CMB}}. \quad (19)$$

We adopt the CMB convention.

### 3 SETUP

We describe in this section the specifications for the different cosmological surveys used in the analysis and the details of the Fisher methodology used to infer uncertainties on  $f_{\text{NL}}$  and  $n_{\text{NL}}$ .

#### 3.1 CMB lensing specifications

We work with a possible CMB-S4 configuration assuming a 3 arcmin beam and  $\sigma_{\text{T}} = \sigma_{\text{P}}/\sqrt{2} = 1 \mu\text{K-arcmin}$  noise (Abazajian et al. 2016). We assume  $\ell_{\text{min}} = 30$  and a different cut at high- $\ell$  of  $\ell_{\text{max}}^{\text{T}} = 3000$  in temperature and  $\ell_{\text{max}}^{\text{P}} = 5000$  in polarization with  $f_{\text{sky}} = 0.4$ .

For temperature and polarization CMB angular power spectra, the instrumental noise deconvolved with the instrumental beam is defined by (Knox 1995)

$$\mathcal{N}_\ell^{\text{T,P}} = \sigma_{\text{T,P}} b_\ell^{-2} \quad (20)$$

where we assume a Gaussian beam

$$b_\ell = \exp \left[ -\ell(\ell + 1) \frac{\theta_{\text{FWHM}}^2}{16 \ln 2} \right]. \quad (21)$$

For CMB lensing, we assume that the lensing reconstruction can be performed with the minimum variance quadratic estimator on the full sky combining the TT, EE, BB, TE, TB, EB CMB estimators calculated according to (Hu & Okamoto 2002) with `quicklens`<sup>1</sup> and applying iterative lensing reconstruction (Hirata & Seljak 2003; Smith et al. 2012). We use the CMB lensing information in the range  $30 \leq \ell \leq 3000$ .

Note that hereafter we will refer to the full set of angular power spectra of the CMB anisotropies (i.e. temperature, E-mode polarization, CMB lensing, and their cross-correlations) by simply saying CMB.

#### 3.2 HI intensity mapping specifications

IM surveys measure the total intensity emission in each pixel for given atomic lines with very accurate redshifts (Battye et al. 2004; Wyithe & Loeb 2008; Chang et al. 2008; Bull et al. 2015; Santos et al. 2015; Kovetz et al. 2017). Without resolving individual galaxies, which act as hosts of the emitting atoms, the measured brightness temperature fluctuations are expected to be a biased tracer of the underlying cold dark matter distribution.

We consider HI emission and we use the fitting formulae from Santos et al. (2017) for the HI linear bias

$$b_{\text{HI}}(z) = \frac{b_{\text{HI}}(0)}{0.677105} \left[ 0.66655 + 0.17765 z + 0.050223 z^2 \right] \quad (22)$$

and for the background HI brightness temperature

$$\bar{T}_{\text{HI}}(z) = 0.055919 + 0.23242 z - 0.024136 z^2 \text{ mK} \quad (23)$$

where  $\Omega_{\text{HI}}(0)b_{\text{HI}}(0) = 4.3 \times 10^{-4}$  and  $\Omega_{\text{HI}}(0) = 4.86 \times 10^{-4}$ .

The noise variance for IM in single dish mode in the  $i$ -frequency channel, assuming scale-independence and no correlation between the noise in different frequency channels, is (Knox 1995; Bull et al. 2015)

$$\sigma_{\text{HI}}(\nu_i) = \frac{4\pi f_{\text{sky}} T_{\text{sys}}^2(\nu_i)}{2N_{\text{dish}} t_{\text{tot}} \Delta\nu}, \quad (24)$$

$$T_{\text{sys}}(\nu) = 25 + 60 \left( \frac{300 \text{ MHz}}{\nu} \right)^{2.55} \text{ K}. \quad (25)$$

<sup>1</sup> <https://github.com/dhanson/quicklens>

We also include the instrumental limit in angular resolution, characterized by the telescope beam. We assume the noise deconvolved with a Gaussian beam modelled as

$$\mathcal{N}_\ell^{\text{HI}}(\nu_i) = \sigma_{\text{HI}} b_\ell^{-2}(\nu_i) \quad (26)$$

where  $b_\ell(\nu_i)$  are the contribution of the beam in the  $i$ -frequency channel given by Eq. (21) with

$$\theta_{\text{FWHM}}(\nu) \approx \frac{c}{\nu D_{\text{dish}}}. \quad (27)$$

For SKA1-MID, we assume  $N_{\text{dish}} = 197$ ,  $D_{\text{dish}} = 15$  m,  $t_{\text{tot}} = 10^4$  hr observing over  $20,000 \text{ deg}^2$  in the redshift range  $0.35 \leq z \leq 3.05$  ( $1050 \geq \nu \geq 350$  MHz, Band 1) (Bacon et al. 2018) divided in 27 tomographic bins with 0.1 width and  $l_{\text{min}} = 5$ .

### 3.3 Galaxy clustering specifications

We present the details of two future photometric galaxy surveys. For each survey we specify the total redshift distribution of sources which follows

$$n_X(z) \propto z^\alpha \exp \left[ - \left( \frac{z}{z_0} \right)^\beta \right], \quad (28)$$

and the linear bias. The distribution of sources in the  $i$ -th redshift bin including photometric uncertainties in the redshift following (Ma et al. 2005) is

$$n_X^i(z) = \int_{z_{\text{ph}}^i}^{z_{\text{ph}}^{i+1}} dz_{\text{ph}} n_X(z) p(z_{\text{ph}}|z) \quad (29)$$

where we adopt a Gaussian distribution for the probability distribution of photometric redshift estimates  $z_{\text{ph}}$  given true redshifts  $z$

$$p(z_{\text{ph}}|z) = \frac{1}{\sqrt{2\pi}\sigma_z} \exp \left[ - \frac{(z - z_{\text{ph}})^2}{2\sigma_z^2} \right]. \quad (30)$$

The shot noise for galaxies corresponds to the inverse of the angular number density of galaxies in the  $i$ -th redshift bin

$$\mathcal{N}_\ell^X = \frac{1}{\bar{n}_X^i} \quad (31)$$

where  $\bar{n}_X^i = \int dz n_X^i(z)$ .

Finally, we impose a cut on small-scales assuming that we will be able to reconstruct non-linear scales up to  $k_{\text{max}} = 0.3 \text{ h/Mpc}$  which reflects to a redshift dependent cut in angular space according to  $\ell_{\text{max}} \approx \chi(z) k_{\text{max}} - 1/2$ .

#### 3.3.1 Euclid-like

The Euclid satellite is a mission of the ESA Cosmic Vision program that will be launched in 2022 (Laureijs et al. 2011). It will perform both a photometric and spectroscopic survey of galaxies. In this work, we focus only on a Euclid-like photometric survey that will probe  $f_{\text{sky}} = 15,000 \text{ deg}^2$  measuring  $\bar{n}_g = 30$  sources per  $\text{arcmin}^2$  over a redshift range  $0 < z < 2.5$  (Amendola et al. 2018).

The redshift distribution of sources for a Euclid-like photometric survey follows Eq. (28) with  $\alpha = 2$ ,  $\beta = 1.5$ , and

$z_0 = 0.636$ , divided into 10 bins each containing the same number of galaxies (Amendola et al. 2018). The scatter of the photometric redshift estimate with respect to the true redshift value is  $\sigma_z = 0.05(1+z)$ , and the galaxy linear bias evolves with redshift following the equation  $b_0(z) = \sqrt{1+z}$  (Amendola et al. 2018). We assume  $l_{\text{min}} = 10$ .

#### 3.3.2 LSST-like

For LSST clustering measurements, we assume a number density of galaxies of  $\bar{n}_g = 48$  sources per  $\text{arcmin}^2$  observed over a patch of the sky of  $f_{\text{sky}} = 13,800 \text{ deg}^2$  and distributed in redshift according to Eq. (28) with  $\alpha = 2$ ,  $\beta = 0.9$ , and  $z_0 = 0.28$  (Alonso et al. 2018).

We assume 10 tomographic bins spaced by 0.1 in photo- $z$  between  $0.2 \leq z \leq 1.2$  with photometric redshift uncertainties  $\sigma_z = 0.03(1+z)$ , and a linear bias  $b_0(z) = 0.95/D(z)$  (Alonso et al. 2018). We assume  $l_{\text{min}} = 20$ .

### 3.4 Fisher analysis

We use the Fisher matrix to derive forecasted constraints on the cosmological parameters assuming that the observed fields were Gaussian random distributed (for simplicity we ignore information from higher-order statistics).

The Fisher matrix at the power spectrum level is then

$$F_{ij} = f_{\text{sky}} \sum_{\ell=\ell_{\text{min}}}^{\ell_{\text{max}}} \left( \frac{2\ell+1}{2} \right) \text{tr} [\mathbf{C}_{\ell,i} \Sigma_\ell \mathbf{C}_{\ell,j} \Sigma_\ell] \quad (32)$$

where  $\mathbf{C}_\ell$  is the covariance matrix,  $\mathbf{C}_{\ell,i} = \partial \mathbf{C}_\ell / \partial \theta_i$  is the derivative with respect to the  $i$ -th element in the cosmological parameter vector  $\boldsymbol{\theta}$ , and  $\Sigma_\ell = (\mathbf{C}_\ell + \mathbf{N}_\ell)^{-1}$  is the inverse of the total noise matrix with  $\mathbf{N}_\ell$  the diagonal noise matrix.

The above equation assumes that all experiments observe the same patch of sky. We consider for each experiment its own sky fraction and for the cross-correlations the smallest of the two sky fractions.

The angular power spectra are (suppressing the redshift dependence)

$$\mathcal{C}_\ell^{\text{XY}} = 4\pi \int \frac{dk}{k} \mathcal{P}_{\mathcal{R}}(k) I_\ell^{\text{X}}(k) I_\ell^{\text{Y}}(k), \quad (33)$$

where  $X, Y = \text{T, E, } \phi, \Delta_g$  or  $\Delta_{\text{HI}}$ . In Eq. (33),  $\mathcal{P}_{\mathcal{R}}$  is the dimensionless primordial power spectrum and the kernels are

$$I_\ell^{\Delta_g}(k, z_i) = \int dz n_X^i(z) \Delta_\ell(k, z) j_\ell(k\chi(z)), \quad (34)$$

$$I_\ell^{\Delta_{\text{HI}}}(k, z_i) = \int dz W_{\text{th}}(z, z_i) \bar{I}_{\text{HI}}(z) \Delta_\ell(k, z) j_\ell(k\chi(z)) \quad (35)$$

where  $W_{\text{th}}(z, z_i)$  is a smoothed top-hat window function for the  $i$ -th bin. We refer the reader to Hu & White (1997) for the details of the CMB temperature and polarization window functions.

All the angular power spectra have been calculated using a modified version of the publicly available code **CAMB**<sup>2</sup> (Lewis et al. 2000; Howlett et al. 2012; Challinor & Lewis 2011).

<sup>2</sup> <https://github.com/cmbant/CAMB>

## 4 RESULTS

The standard cosmological parameter vector that we use reads

$$\theta = \{\omega_b, \omega_c, H_0, \tau, \ln(10^{10} A_s), n_s\}. \quad (36)$$

In addition, we have the PNG parameters depending on the model studied:  $\{f_{\text{NL}}\}$  or  $\{f_{\text{NL}}, n_{\text{NL}}\}$ . Moreover, we include a nuisance parameter per redshift bin for each of the LSS surveys, thus allowing for a free redshift evolution of the clustering bias  $b_0$  or of the combination  $\bar{T}_{\text{HI}} b_{\text{HI}}$  for IM.

The fiducial cosmology assumed for the standard cosmological parameters, according to *Planck* 2018 (Aghanim et al. 2018a), is  $\omega_b = 0.022383$ ,  $\omega_c = 0.12011$ ,  $H_0 = 67.32$ ,  $\tau = 0.0543$ ,  $\ln(10^{10} A_s) = 3.0448$ ,  $n_s = 0.96605$ . We assume  $f_{\text{NL}} = 0$  without running and  $f_{\text{NL}} = -0.9$ ,  $n_{\text{NL}} = 0$  for the extended model.

Uncertainties reported in the following subsections have been marginalized over all the standard cosmological parameters and all the nuisance bias parameters.

### 4.1 $f_{\text{NL}}$ -model

We consider different minimum multipoles as feasible for the different experimental configurations described in section 3. In figure 1, we present the uncertainties on  $f_{\text{NL}}$  by changing  $\ell_{\text{min}}$ .

The uncertainties for this model correspond to  $\sigma(f_{\text{NL}}) \approx 2.1$  for SKA1-MID IM with  $\ell_{\text{min}} = 5$ ,  $\sigma(f_{\text{NL}}) \approx 2.3$  for Euclid-like with  $\ell_{\text{min}} = 10$ , and  $\sigma(f_{\text{NL}}) \approx 16.2$  for LSST-like with  $\ell_{\text{min}} = 20$ .

Including CMB lensing from CMB-S4 with  $\ell_{\text{min}} = 30$ , the errors decrease to  $\sigma(f_{\text{NL}}) \approx 1.6$ , 1.8, 10.5 for SKA1-HI IM, Euclid-like, and LSST-like, respectively. Whereas the combination between intensity and number counts leads to  $\sigma(f_{\text{NL}}) \approx 0.96$  for SKA1-MID IM in combination with Euclid-like and  $\sigma(f_{\text{NL}}) \approx 1.6$  for SKA1-MID IM in combination with LSST-like.

Once all three tracers are included, the tightest constraint of  $\sigma(f_{\text{NL}}) \approx 0.9$  is obtained by the combination CMB  $\times$  SKA1-MID IM  $\times$  Euclid-like, with corresponding minimum multipoles [30, 5, 10], respectively. By using LSST-like, we obtain  $\sigma(f_{\text{NL}}) \approx 1.4$ .

In addition, we investigate the case where the minimum multipoles extend to 2 for all three tracers. These yield the following constraints for the multi-tracer cases:  $\sigma(f_{\text{NL}}) \approx 0.47$  for CMB  $\times$  SKA1-MID IM  $\times$  Euclid-like and  $\sigma(f_{\text{NL}}) \approx 1.0$  for CMB  $\times$  SKA1-MID IM  $\times$  LSST-like.

### 4.2 $n_{\text{NL}}$ -model

We discuss now the constraints for the two-parameter model (2) with a running of  $f_{\text{NL}}$ . In figure 2, we show the marginalized uncertainties on the 2-dimensional  $f_{\text{NL}}-n_{\text{NL}}$  parameter space.

The uncertainties for this model correspond to  $\sigma(n_{\text{NL}}) \approx 2.7$  for SKA1-MID IM,  $\sigma(n_{\text{NL}}) \approx 0.35$  for Euclid-like, and  $\sigma(n_{\text{NL}}) \approx 0.37$  for LSST-like.

Including CMB lensing from CMB-S4 with  $\ell_{\text{min}} = 30$ , errors decrease to  $\sigma(n_{\text{NL}}) \approx 1.4$ , 0.24, 0.32 for SKA1-HI IM, Euclid-like, and LSST-like, respectively. Whereas the

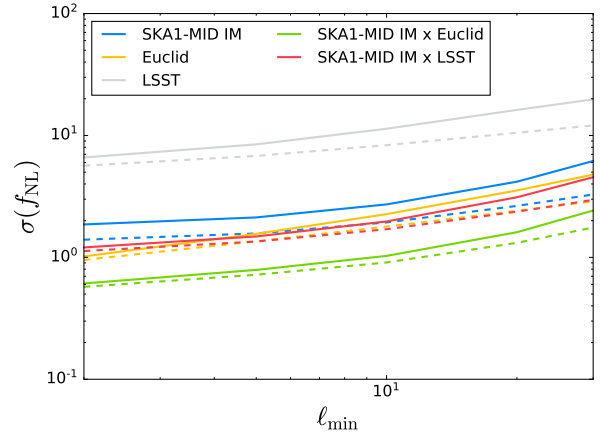


**Figure 1.** Marginalized uncertainties on  $f_{\text{NL}}$  as function of the minimum multipole  $\ell_{\text{min}}$  of LSS. Solid curves correspond to single LSS experiment without CMB: SKA1-MID IM (blue), Euclid-like (yellow), and LSST-like (gray). Dashed lines correspond to the combination of the CMB with LSS fixing  $\ell_{\text{min}} = 30$  for the CMB.

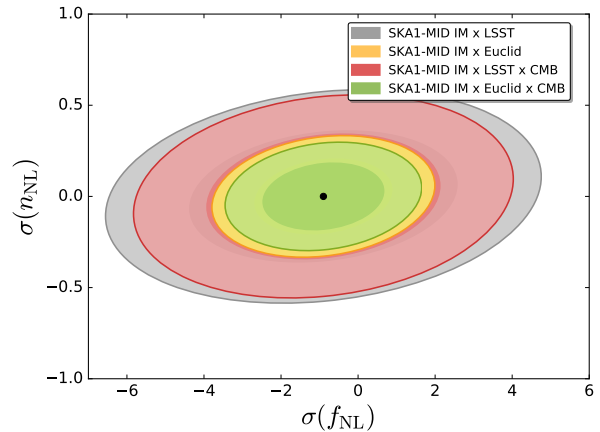


**Figure 2.** Marginalized 2-dimensional constraint plots for  $f_{\text{NL}}$  versus  $n_{\text{NL}}$  in the case of  $\ell_{\text{min}} = 5, 10, 30$  for HI IM, galaxy number counts, and CMB respectively. The contours correspond to the 68% and 95% CL, with SKA1-MID IM combined Euclid-like (yellow), SKA1-MID IM combined LSST-like (grey), CMB  $\times$  SKA1-MID IM  $\times$  Euclid-like (green), and CMB  $\times$  SKA1-MID IM  $\times$  LSST-like (red).

combination between intensity and number counts leads to  $\sigma(n_{\text{NL}}) \approx 0.13$  for SKA1-MID IM in combination with Euclid-like and  $\sigma(n_{\text{NL}}) \approx 0.24$  for SKA1-MID IM in combination with LSST-like.

Once all three tracers are included, the tightest constraint of  $\sigma(n_{\text{NL}}) \approx 0.12$  is obtained by the combination of CMB  $\times$  SKA1-MID IM  $\times$  Euclid-like. By using LSST-like, we obtain  $\sigma(n_{\text{NL}}) \approx 0.22$ .

In this case the uncertainties on  $f_{\text{NL}}$  degrade by  $\sim 20\%$  on average, compared to the case without running, which shows a weak degeneracy between the two parameters.

### 4.3 Comparison with other works

We discuss in this subsection the differences between our findings with some uncertainties on  $f_{\text{NL}}$  derived in literature. In this work, we consistently make use of the CMB convention to define  $f_{\text{NL}}$ . In comparison with other works where the alternate LSS convention is used, we quote here the relevant constraints modified to be consistent with the CMB convention (19) which we use.

In [Alonso et al. \(2015\)](#) and [Alonso & Ferreira \(2015\)](#) the case of LSST-like and SKA1-MID IM is dealt with, giving uncertainties down to  $\sim 0.31$  in cross-correlation. Here, the SKA1-MID IM survey is split into a greater number of thinner bins: 100 bins with equal co-moving width. In addition, 9 bins are used for LSST-like, with widths chosen to ensure equal source density, as opposed to our 10 fixed-width bins. The multipole range considered is  $[2, 500]$  for both tracers. The sky fractions used are larger than ours: 0.5 for LSST-like and 0.75 for SKA1, with the overlap taken as 0.4, which also exceeds ours. The redshift distribution is normalised to a slightly more pessimistic 40 sources/arcmin<sup>2</sup>, versus our 48 sources/arcmin<sup>2</sup> according to [Alonso et al. \(2018\)](#) which results in a slightly lower shot noise.

In [Fonseca et al. \(2015\)](#) there are two cases that deal with Euclid-like and SKA1-MID IM, considering (i) a 50% overlap and (ii) complete overlap between the different survey areas of these two tracers. Multi-tracer results for  $\sigma(f_{\text{NL}})$  are between (0.72 and 1.05) depending on the maximum multipole chosen ( $\ell_{\text{max}} = 60$  or  $\ell_{\text{max}} = 300$ ) and the sky overlap (50% or 100%). The third case (iii) considers the LSST-like with a survey area equal to that of the entire SKA1-MID IM. Here, the multi-tracer result for  $\ell_{\text{max}} = 300$  is  $\sigma(f_{\text{NL}}) \simeq 0.61$ . The multipole range chosen for both tracers extends down to  $\ell_{\text{min}} = 2$ , while the maximum multipole is lower than ours:  $\ell_{\text{max}} = 300$ . Considering that the effect of  $f_{\text{NL}}$  is captured only on larger scales, this difference in  $\ell_{\text{max}}$  should have a negligible effect on the final uncertainties. There are 20 bins for both surveys, chosen so that there are equal number counts of Euclid-like sources in each. The sky fraction in case (i) the 50% overlap of 0.18 is smaller than our shared sky fraction of 0.36 for SKA1-MID IM and Euclid-like. However, the SKA1 sky fraction used in the three cases is 0.72, which is larger than our 0.48 according to [Bacon et al. \(2018\)](#). In case (iii) the LSST-like sky fraction is also chosen as 0.72, larger than our sky fraction for LSST-like of  $\sim 0.33$  according to [Alonso et al. \(2018\)](#). The bias fitting functions used are the same as ours, and the same kind of nuisance parameters are introduced.

In [Schmittfull & Seljak \(2018\)](#), the case of LSST-like clustering and CMB-S4 lensing in cross correlation is investigated. The uncertainties found are  $\sigma(f_{\text{NL}}) \simeq 0.4$  or  $\sigma(f_{\text{NL}}) \simeq 1.0$  for the cases where the minimum multipole for both tracers is either 2 or 20, respectively. They split the galaxy redshift distribution into 6 bins, extending over a larger redshift range from 0 to 7 and assuming a redshift distribution normalised to 50 sources/arcmin<sup>2</sup>. The sky fractions used to obtain these results are 0.5 for CMB and LSST, assuming 100% overlap. The bias for LSST is calculated according to the model  $b_0(z) = 1 + z$  as opposed to the one we use with  $b_0(z) = 0.95/D(z)$ .

Note the our results for LSST-like are weaker than the uncertainties for Euclid-like and weaker compared to the un-

certainties in literature mainly for the sky fraction assumed according to ([Alonso et al. 2018](#)) and not for the smaller redshift range considered.

In light of the differences in assumptions made in the literature compared to this work, it is not unexpected that our constraints are not always tighter than those from previous investigations. However, it must be stressed that our constraints use conservative estimates and the most up-to-date specifications for the surveys involved.

## 5 CONCLUSIONS

In this paper we have shown how more than one tracer of the cosmic density field can be used to extract precise measurements of perturbations on scales beyond the equality scale. We have shown that a conservative combination of a 21 cm IM survey from SKA1-MID with photometric galaxy surveys and with CMB lensing from CMB-S4 will allow us to obtain uncertainties for PNG parameters of  $\sigma(f_{\text{NL}}) \lesssim 0.9$  and  $\sigma(n_{\text{NL}}) \lesssim 0.2$ . We highlight the importance on CMB lensing information through the cross-correlation with intensity/ number counts to further improve the uncertainties on  $f_{\text{NL}}$ .

The uncertainties for the local type non-Gaussianity correspond to  $\sigma(f_{\text{NL}}) \simeq 2.1$  for SKA1-MID IM with  $\ell_{\text{min}} = 5$ ,  $\sigma(f_{\text{NL}}) \simeq 2.3$  for Euclid-like with  $\ell_{\text{min}} = 10$ , and  $\sigma(f_{\text{NL}}) \simeq 16.2$  for LSST-like with  $\ell_{\text{min}} = 20$ ; on the running index of  $f_{\text{NL}}$  we find  $\sigma(n_{\text{NL}}) \simeq 2.7, 0.35, 0.37$  respectively. We combine the different galaxy surveys via the multi-tracer approach. This leads to  $\sigma(f_{\text{NL}}) \simeq 0.96$  (1.6) by combining SKA1-MID IM with Euclid-like (LSST-like) and  $\sigma(n_{\text{NL}}) \simeq 0.13$  (0.24).

Then we go further and include CMB information from a possible CMB-S4 ground-based experiment in the multi-tracer. Including CMB from CMB-S4 with  $\ell_{\text{min}} = 30$ , errors decrease to  $\sigma(f_{\text{NL}}) \simeq 1.6, 1.8, 10.5$  for SKA1-HI IM, Euclid-like, and LSST-like, respectively. Once all three tracers are included, the tightest uncertainties of  $\sigma(f_{\text{NL}}) \simeq 0.90$  and  $\sigma(n_{\text{NL}}) \simeq 0.12$  are obtained by the combination of SKA1-MID IM, Euclid-like, and CMB. By using LSST-like instead of Euclid-like, we obtain  $\sigma(f_{\text{NL}}) \simeq 1.4$  and  $\sigma(n_{\text{NL}}) \simeq 0.22$ .

We consider also the possibility of using simulated *Planck*-like data, leading to uncertainties on the cosmological parameters compatible with the latest results in ([Akrami et al. 2018](#); [Aghanim et al. 2018a,b](#)) as representative of current CMB measurements. In this case, the improvement in uncertainties by adding *Planck* to single tracer is very small and mostly due to parameter degeneracy with the standard cosmological parameters rather than an imprinting of  $f_{\text{NL}}$  on the cross-correlation between intensity/number counts with CMB lensing. We also test the possibility of completing the missing first multipoles  $2 \leq \ell_{\text{min}} < 30$  in the CMB spectra without finding any further improvement.

Constraints on PNG parameters from the measure of ultra-large scales depend strongly on the  $\ell_{\text{min}}$  and  $f_{\text{sky}}$  considered in the analysis. We assumed the corresponding minimum multipoles for each experiment according to up-to-date specifications for each survey:  $\ell_{\text{min}} = 5$  for SKA1-MID IM ([Bacon et al. 2018](#)),  $\ell_{\text{min}} = 10$  for Euclid-like ([Amendola et al. 2018](#)),  $\ell_{\text{min}} = 20$  for LSST-like ([Alonso et al. 2018](#)), and  $\ell_{\text{min}} = 30$  for CMB-S4 ([Abazajian et al. 2016](#)). We also study

how uncertainties get worse as a function of the minimum multipole in Fig. 1.

Regarding the surveys' sky fraction, we assume 20,000 deg<sup>2</sup> for SKA1-MID IM, 15,000 deg<sup>2</sup> for Euclid-like, 13,800 deg<sup>2</sup> for LSST-like, 16,500 deg<sup>2</sup> for CMB-S4, and the smallest of the two sky fractions for the cross-correlations. In case of smaller overlap, uncertainties will be mildly negatively affected.

Finally, many other different tracers have been highlighted as good candidates to obtain competitive constraints on  $f_{\text{NL}}$ , such as clusters of galaxies (Pillepich et al. 2012; Mana et al. 2013; Sartoris et al. 2016), cosmic infrared background (Tucci et al. 2016), cosmic voids (Chan et al. 2018) and different IM lines like H $\alpha$ , CO and [CII] (Fonseca et al. 2018; Moradinezhad Dizgah & Keating 2019). These might also be included in the analysis in order to reach more robust and tighter constraints.

## ACKNOWLEDGEMENTS

The authors were supported by the South African Radio Astronomy Observatory, which is a facility of the National Research Foundation, an agency of the Department of Science and Technology (Grant. No. 75415). MB was also supported by the Claude Leon Foundation and by ASI n.I/023/12/0 "Attività relativa alla fase B2/C per la missione Euclid". RM was also supported by the UK Science & Technology Facilities Council (Grant no. ST/N000668/1).

## REFERENCES

Abazajian K. N., et al., 2016. ([arXiv:1610.02743](#))  
 Abramo L. R., Bertacca D., 2017, *Phys. Rev.*, D96, 123535  
 Abramo L. R., Leonard K. E., 2013, *Mon. Not. Roy. Astron. Soc.*, 432, 318  
 Acquaviva V., Bartolo N., Matarrese S., Riotto A., 2003, *Nucl. Phys.*, B667, 119  
 Aghanim N., et al., 2018a. ([arXiv:1807.06209](#))  
 Aghanim N., et al., 2018b. ([arXiv:1807.06210](#))  
 Akrami Y., et al., 2018. ([arXiv:1807.06205](#))  
 Akrami Y., et al., 2019. ([arXiv:1905.05697](#))  
 Albrecht A., Steinhardt P. J., 1982, *Phys. Rev. Lett.*, 48, 1220  
 Alonso D., Ferreira P. G., 2015, *Phys. Rev.*, D92, 063525  
 Alonso D., Bull P., Ferreira P. G., Maartens R., Santos M., 2015, *Astrophys. J.*, 814, 145  
 Alonso D., et al., 2018. ([arXiv:1809.01669](#))  
 Amendola L., et al., 2018, *Living Rev. Rel.*, 21, 2  
 Bacon D. J., et al., 2018. ([arXiv:1811.02743](#))  
 Ballardini M., Finelli F., Fedeli C., Moscardini L., 2016, *JCAP*, 1610, 041  
 Bartolo N., Komatsu E., Matarrese S., Riotto A., 2004, *Phys. Rept.*, 402, 103  
 Battye R. A., Davies R. D., Weller J., 2004, *Mon. Not. Roy. Astron. Soc.*, 355, 1339  
 Becker A., Huterer D., 2012, *Phys. Rev. Lett.*, 109, 121302  
 Bull P., Ferreira P. G., Patel P., Santos M. G., 2015, *Astrophys. J.*, 803, 21  
 Byrnes C. T., Choi K.-Y., 2010, *Adv. Astron.*, 2010, 724525  
 Camera S., Santos M. G., Ferreira P. G., Ferramacho L., 2013, *Phys. Rev. Lett.*, 111, 171302  
 Castorina E., et al., 2019. ([arXiv:1904.08859](#))  
 Challinor A., Lewis A., 2011, *Phys. Rev.*, D84, 043516  
 Chan K. C., Hamaus N., Biagetti M., 2018. ([arXiv:1812.04024](#))

Chang T.-C., Pen U.-L., Peterson J. B., McDonald P., 2008, *Phys. Rev. Lett.*, 100, 091303  
 Chen X., 2005, *Phys. Rev.*, D72, 123518  
 Chen X., 2010, *Adv. Astron.*, 2010, 638979  
 Chen X., Namjoo M. H., Wang Y., 2015, *JCAP*, 1502, 027  
 Creminelli P., Zaldarriaga M., 2004, *JCAP*, 0410, 006  
 Dalal N., Doré O., Huterer D., Shirokov A., 2008, *Phys. Rev.*, D77, 123514  
 Desjacques V., Seljak U., Iliev I., 2009, *Mon. Not. Roy. Astron. Soc.*, 396, 85  
 Desjacques V., Jeong D., Schmidt F., 2018, *Phys. Rept.*, 733, 1  
 Ferramacho L. D., Santos M. G., Jarvis M. J., Camera S., 2014, *Mon. Not. Roy. Astron. Soc.*, 442, 2511  
 Ferraro S., Smith K. M., 2015, *Phys. Rev.*, D91, 043506  
 Fonseca J., Camera S., Santos M., Maartens R., 2015, *Astrophys. J.*, 812, L22  
 Fonseca J., Maartens R., Santos M. G., 2017, *Mon. Not. Roy. Astron. Soc.*, 466, 2780  
 Fonseca J., Maartens R., Santos M. G., 2018, *Mon. Not. Roy. Astron. Soc.*, 479, 3490  
 Gangui A., Lucchin F., Matarrese S., Mollerach S., 1994, *Astrophys. J.*, 430, 447  
 Guth A. H., 1981, *Phys. Rev.*, D23, 347  
 Hawking S. W., Moss I. G., Stewart J. M., 1982, *Phys. Rev.*, D26, 2681  
 Hirata C. M., Seljak U., 2003, *Phys. Rev.*, D68, 083002  
 Howlett C., Lewis A., Hall A., Challinor A., 2012, *JCAP*, 1204, 027  
 Hu W., Okamoto T., 2002, *Astrophys. J.*, 574, 566  
 Hu W., White M. J., 1997, *Phys. Rev.*, D56, 596  
 Knox L., 1995, *Phys. Rev.*, D52, 4307  
 Kovetz E. D., et al., 2017. ([arXiv:1709.09066](#))  
 Laureijs R., et al., 2011. ([arXiv:1110.3193](#))  
 Lewis A., Challinor A., Lasenby A., 2000, *Astrophys. J.*, 538, 473  
 Li X., Weaverdyck N., Adhikari S., Huterer D., Muir J., Wu H.-Y., 2018, *Astrophys. J.*, 862, 137  
 Linde A. D., 1982, *Phys. Lett.*, 108B, 389  
 Linde A. D., 1983, *Phys. Lett.*, 129B, 177  
 Ma Z.-M., Hu W., Huterer D., 2005, *Astrophys. J.*, 636, 21  
 Maldacena J. M., 2003, *JHEP*, 05, 013  
 Mana A., Giannantonio T., Weller J., Hoyle B., Huetsi G., Sartoris B., 2013, *Mon. Not. Roy. Astron. Soc.*, 434, 684  
 Matarrese S., Verde L., 2008, *Astrophys. J.*, 677, L77  
 Mifsud J., van de Bruck C., 2019  
 Mo H. J., White S. D. M., 1996, *Mon. Not. Roy. Astron. Soc.*, 282, 347  
 Moradinezhad Dizgah A., Keating G. K., 2019, *Astrophys. J.*, 872, 126  
 Muñoz J. B., Kovetz E. D., Raccanelli A., Kamionkowski M., Silk J., 2017, *JCAP*, 1705, 032  
 Mukhanov V. F., Chibisov G. V., 1981, *JETP Lett.*, 33, 532  
 Oppizzi F., Liguori M., Renzi A., Arroja F., Bartolo N., 2018, *JCAP*, 1805, 045  
 Pillepich A., Porciani C., Reiprich T. H., 2012, *Mon. Not. Roy. Astron. Soc.*, 422, 44  
 Raccanelli A., Dore O., Dalal N., 2015, *JCAP*, 1508, 034  
 Salopek D. S., Bond J. R., 1990, *Phys. Rev.*, D42, 3936  
 Santos M., et al., 2015, in Proceedings, Advancing Astrophysics with the Square Kilometre Array (AASKA14): Giardini Naxos, Italy, June 9-13, 2014. p. 019, [doi:10.22323/1.215.0019](#)  
 Santos M. G., et al., 2017, in Proceedings, MeerKAT Science: On the Pathway to the SKA (MeerKAT2016): Stellenbosch, South Africa, May 25-27, 2016. ([arXiv:1709.06099](#))  
 Sartoris B., et al., 2016, *Mon. Not. Roy. Astron. Soc.*, 459, 1764  
 Sato K., 1981, *Mon. Not. Roy. Astron. Soc.*, 195, 467  
 Schmidt F., Kamionkowski M., 2010, *Phys. Rev.*, D82, 103002  
 Schmittfull M., Seljak U., 2018, *Phys. Rev.*, D97, 123540

- Sefusatti E., Liguori M., Yadav A. P. S., Jackson M. G., Pajer E., 2009, *JCAP*, 0912, 022
- Seljak U., 2009, *Phys. Rev. Lett.*, 102, 021302
- Sheth R. K., Tormen G., 1999, *Mon. Not. Roy. Astron. Soc.*, 308, 119
- Slosar A., Hirata C., Seljak U., Ho S., Padmanabhan N., 2008, *JCAP*, 0808, 031
- Smith K. M., Hanson D., LoVerde M., Hirata C. M., Zahn O., 2012, *JCAP*, 1206, 014
- Starobinsky A. A., 1980, *Phys. Lett.*, B91, 99
- Tucci M., Desjacques V., Kunz M., 2016, *Mon. Not. Roy. Astron. Soc.*, 463, 2046
- Wyithe S., Loeb A., 2008, *Mon. Not. Roy. Astron. Soc.*, 383, 606
- Yamauchi D., Takahashi K., Oguri M., 2014, *Phys. Rev.*, D90, 083520
- Yoo J., Hamaus N., Seljak U., Zaldarriaga M., 2012, *Phys. Rev.*, D86, 063514
- de Putter R., Doré O., 2017, *Phys. Rev.*, D95, 123513